Chest computed tomography radiomics to predict the outcome for patients with COVID-19 at an early stage

Shan Wu 🆔
Ranying Zhang 🆔
Xinjian Wan 🆔
Ting Yao 🆔
Qingwei Zhang 🆔
Xiaohua Chen 🆔
Xiaohong Fan 🆔

Shan Wu and Ranying Zhang contributed equally to this work.

From the Department of Endoscopy, (S.W., X.W.) Shanghai Sixth People's Hospital Affiliated to Shanghai Jiao Tong University School of Medicine, Shanghai, China; Department of Radiology (R.Z.), Zhongshan Hospital, Fudan University, and Shanghai Institute of Medical Imaging, Shanghai, China; Department of Infectious Disease (T.Y., X.C. ✉chenxiaohua2000@163.com), Shanghai Sixth People's Hospital Affiliated to Shanghai Jiao Tong University School of Medicine, Shanghai, China; Division of Gastroenterology and Hepatology (Q.Z. ✉zhangqingweif@hotmail.com), Key Laboratory of Gastroenterology and Hepatology, Ministry of Health, Renji Hospital, School of Medicine, Shanghai Jiao Tong University, Shanghai Institute of Digestive Disease, Shanghai, China; Department of Respiratory Medicine, Shanghai Sixth People's Hospital Affiliated to Shanghai Jiao Tong University School of Medicine; Department of Respiratory and Critical Care (X.F. ✉fanxiaohong@shphc.org.cn), Shanghai Public Health Clinical Center, Fudan University, Shanghai, China.

PURPOSE

Early monitoring and intervention for patients with novel coronavirus disease-2019 (COVID-19) will benefit both patients and the medical system. Chest computed tomography (CT) radiomics provide more information regarding the prognosis of COVID-19.

METHODS

A total of 833 quantitative features of 157 COVID-19 patients in the hospital were extracted. By filtering unstable features using the least absolute shrinkage and selection operator algorithm, a radiomic signature was built to predict the prognosis of COVID-19 pneumonia. The main outcomes were the area under the curve (AUC) of the prediction models for death, clinical stage, and complications. Internal validation was performed using the bootstrapping validation technique.

RESULTS

The AUC of each model demonstrated good predictive accuracy [death, 0.846; stage, 0.918; complication, 0.919; acute respiratory distress syndrome (ARDS), 0.852]. After finding the optimal cut-off for each outcome, the respective accuracy, sensitivity, and specificity were 0.854, 0.700, and 0.864 for the prediction of the death of COVID-19 patients; 0.814, 0.949, and 0.732 for the prediction of a higher stage of COVID-19; 0.846, 0.920, and 0.832 for the prediction of complications of COVID-19 patients; and 0.814, 0.818, and 0.814 for ARDS of COVID-19 patients. The AUCs after bootstrapping were 0.846 [95% confidence interval (CI): 0.844–0.848] for the death prediction model, 0.919 (95% CI: 0.917–0.922) for the stage prediction model, 0.919 (95% CI: 0.916–0.921) for the complication prediction model, and 0.853 (95% CI: 0.852–0.0.855) for the ARDS prediction model in the internal validation. Based on the decision curve analysis, the radiomics nomogram was clinically significant and useful.

CONCLUSION

The radiomic signature from the chest CT was significantly associated with the prognosis of COVID-19. A radiomic signature model achieved maximum accuracy in the prognosis prediction. Although our results provide vital insights into the prognosis of COVID-19, they need to be verified by large samples in multiple centers.

KEYWORDS

Radiomic signature, prognosis, COVID-19, prediction

The novel coronavirus disease-2019 (COVID-19) has caused a global pandemic, which presents a threat to human health. The COVID-19 infection causes a fever, cough, and diarrhea, among other symptoms. It can affect several tissues, lead to rapid organ failure, and has a poor prognosis and high mortality rate. Once patients progress to a severe stage of pneumonia, over 60% of them die.[1] To date, there is no effective treatment for COVID-19. However, early diagnosis, immediate patient isolation, and extensive vaccination could effectively prevent the transmission of the SARS-CoV-2 virus.[2] Accurate predictive models are needed to identify the risk of patients experiencing a poor clinical outcome and plan early intervention to improve outcomes.[3-5]

A chest computed tomography (CT) scan combined with a positive molecular polymerase chain reaction (PCR) test is the most important diagnostic method for COVID-19. Compared with the test conducted in standard laboratories, the CT scan procedure has a faster turnaround time and can provide more detailed information about the prognostic significance of the severity of lung damage. Several studies on quantitative CT radiomics or deep-learning techniques have shown the efficiency of a rapid diagnosis of COVID-19.[6,7] It is unknown whether quantitative CT radiomics could provide more information for patients. The quantitative image provides data on clinical decisions and prediction prognoses in many fields,[8,9] and radiomics provide more detailed information on the severity of the lung damage and prognosis of patients with COVID-19.

In this paper, we have developed a radiomics prediction model, a novel tool that extracts hundreds of quantitative features based on the shape, intensity, size, or volume of the target lesions, to predict the outcomes of COVID-19.

Methods

Patients

We retrospectively analyzed 157 patients with confirmed positive results of COVID-19 from a viral nucleic acid reverse transcription-PCR test of respiratory secretions via a nasopharyngeal or oropharyngeal swab in Wuhan Leishenshan Hospital. The Ethics Committee of Shanghai Sixth's People's Hospital approved this retrospective study, and written informed consent was waived (approval no.: 2020-KY-013).

All patients' first CT scans after hospitalization were included (Incisive CT, Philips Healthcare and Revolution Maxima, GE Healthcare). The scanning range was from the apex to the lung base. The main scanning parameters were as follows: tube voltage = 120 kVp, tube current = 360 mAs/287 mAs, matrix = 512 × 512, slice thickness = 5 mm, spacing between slices = 5 mm, field of view = 350 mm × 350 mm, window level = 600 Hounsfield units (HU), and window width = 1.200 HU.

Clinical variables and the primary outcome

Clinical data were collected, including the clinical signs and symptoms (fever, headache, cough, expectoration, fatigue, dyspnea, nausea and vomiting, diarrhea, arthralgia, and myalgia), imaging results, demographic variables (age, sex, smoking status, and time between onset of symptoms to admission), and medical history (comorbidities, respiratory diseases, diabetes, hypertension, coronary artery disease, cerebrovascular disease, cancer, and chronic renal disease).

The primary endpoint in the study was efficacy in the predictions of death, clinical stage, and complications. Complications, including stroke, acute kidney injury, acute respiratory distress syndrome (ARDS), and heart failure, which appeared secondary to pneumonia, were defined as positive if the patient had one or more of these complications.

Image segmentation and blinding

All non-contrasted CT images were performed using ITK-SNAP software (version 2.2.0; www.itksnap.org) for manual segmentation of the regions of interest (ROIs). Since the presence of lesions interfered with the automatic identification of the chest, we manually delineated along the edge of the pulmonary parenchyma, slice by slice, for each patient. A three-dimensional ROI of the whole lung was then automatically generated by the software. The hilus pulmonis and the trachea were also included in the ROI (Figure 1). All the images were evaluated by two experienced radiologists who were blinded to the patients' clinical information (Ran-ying Zhang, Reader 1, with seven years of radiologist experience; Ting Yao, Reader 2, with four years of experience).

Radiomic signature building

Figure 1 demonstrates our workflow. The radiomic features were extracted from each ROI using PyRadiomics on Python (version 3.7).[10] Before extraction, all the chest CT images were subjected to image normalization (the intensity of the image was scaled to 0–500). During the normalization process, the binwidth was set to 25, and the intensity of the image of from 1 to 25 bin, 26 to 50, 51 to 75 and so on was regarded as the same intensity in avoid of diversity due to the different parameter setting of CT machine and personal difference. Then, the normalized image was resampled to the same resolution (1 mm × 1 mm × 1 mm) using the interpolation method of sitkBSpline to avoid any
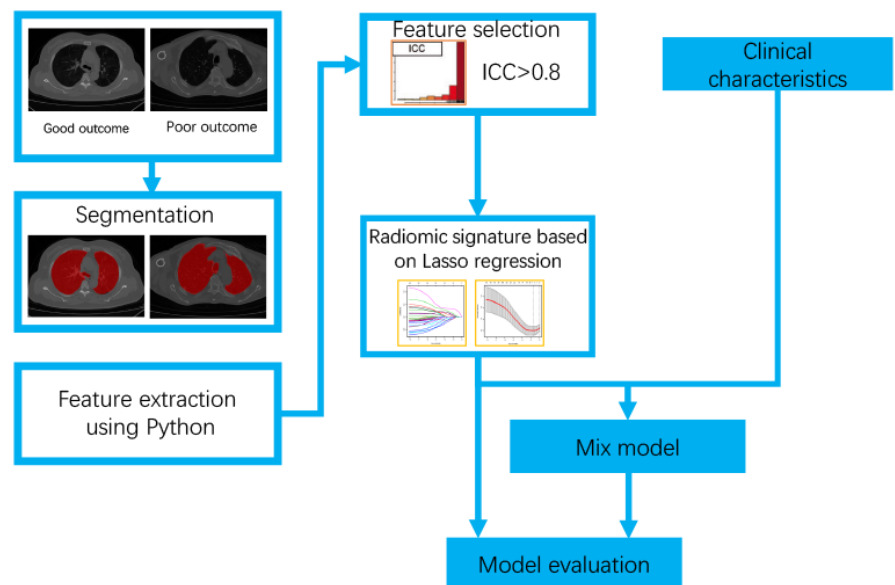
Figure 1. Schematic diagram of the proposed workflow. ICC, inter-class correlation coefficient.

possible data heterogeneity. This procedure was followed by a filtering process to implement image smoothing. After filtering, the radiomic features were extracted from the ROI of the original image and its corresponding filtered results, which included features of first-order statistics, shape, grey-level co-occurrence matrix, grey-level run-length matrix, grey-level size-zone matrix, gray-level dependence matrix, and wavelet features.

The radiomic features of all patients were standardized using the z-score method. Intra-/inter-class correlation coefficients (ICCs) were calculated for each extracted radiomic feature, and those with ICCs of >0.8 were selected. In addition, we calculated the P value of the paired t-test for radiomic features with ICCs of >0.8. We chose the least absolute shrinkage and selection operator (LASSO) algorithm to complete the radiomic signature building and form radiomic models with features of non-zero regression coefficients. Each endpoint (stage, death, complication, respiratory failure) had a corresponding model. In total, four radiomic models were constructed to predict the occurrence of the endpoints.

To build a predictive radiomics model for each outcome, we followed several steps. First, the method of normalization to z distribution [(value − mean value)/standard deviation] was applied for each extracted feature. Second, the ICCs were calculated for each extracted radiomic feature, and those with ICCs of >0.8 were selected. Third, the LASSO algorithm was applied for further feature reduction. The most significant features with the smallest deviance were then selected using the LASSO algorithm for the final features. The LASSO algorithm is a penalized regression method that has been successfully applied to oncologic research. The LASSO algorithm can estimate the regression coefficients by maximizing the log-likelihood function (or the sum of squared residuals) with the constraint, reduce the coefficients of indistinctive covariates to zero, and enable the non-zero features to be combined into a radiomics model.[11,12] With this model, the risk score for each patient was calculated using the following formula weighted by regression coefficients for each outcome: risk score = constant + coefficients × features.

Statistical analysis

The predictive accuracy of the radiomic signature was evaluated using a receiver operating characteristic curve analysis. To determine the optimal cut-off value to pre-dict each outcome, the Youden index was calculated for all possible cut-off values (c) [(Youden index = maxc (sensitivity + specificity − 1)],[13] and the value of c that achieves the maximized index was considered optimal. For each model, the accuracy, sensitivity, and specificity were also measured using the defined optimal cut-off values. For internal validation, the corrected area under the curve (AUC) was calculated using bootstrapping validation (1,000 bootstrap resamples).[14] In addition, a decision curve analysis (DCA) was performed to evaluate the clinical usefulness of the radiomic signature by quantifying the net benefit at different threshold probabilities.[15]

To explore the clinical utility of the addition of a radiomics signature for each outcome to the models with only clinical data included, we first constructed the clinical model using stepwise backward regression. We initially included the demographics of patients, their symptoms, and their past medical history by calculating the AUC for each outcome. Then, the AUC was calculated for the mixed models by including the clinical models and radiomics signature. Meanwhile, the net reclassification index (NRI), an alternative to AUC to assess the improvement in risk prediction and measure the usefulness of a new model,[16] was calculated to evaluate the clinical benefits and utility of the mixed models compared with the clinical models. A statistical analysis was performed using R software (version 3.5.0, packages: irr, caret, glmnet, caTools, OptimalCutpoints, rms, rmda), and $P < 0.05$ was considered statistically significant.[17]

Results

Patient characteristics

We collected data from 157 patients in Wuhan Leishenshan Hospital between February 19, 2020, and April 10, 2020. The mean (standard deviation) age of these patients was 63.13 (14.14), and 86 of them were women (55.13%). At hospital admission, 59 patients were severe, and 25 patients had severe complications. The overall mortality was 6.3% (Table 1).

Feature selection and radiomic signature building

For each ROI, a total of 833 quantitative features were extracted. Using an ICC of 0.80 as a cut-off for determining good reproducibility, a total of 257 radiomic features were selected for the next assessment. As shown in Supplementary Table 1, almost all the P values of the paired t-test for radiomic features for all 257 radiomic features were larger than 0.05. After applying the LASSO logistic algorithm, 60 radiomic features were used to develop all the radiomic models.

As shown in Table 2, the AUC of each model demonstrated good predictive accuracy (death model, 0.846; stage model, 0.918; complications model, 0.919; ARDS model, 0.852). After finding the optimal cut-off for each outcome, the respective accuracy, sensitivity, and specificity were 0.854, 0.700, and 0.864 for the prediction of death of COVID-19 patients; 0.814, 0.949, and 0.732 for the prediction of higher-stage COVID-19; 0.846, 0.920, and 0.832 for the prediction of complications of COVID-19 patients; and 0.814, 0.818, and 0.814 for ARDS of COVID-19 patients. The AUCs after bootstrapping were 0.846 for the death prediction model, 0.919 for the stage prediction model, 0.919 for the complications prediction model, and 0.853 for the ARDS prediction model in the internal validation, which indicates that the models were stable. The DCA for the four radiomic models with different endpoints is presented in Figure 2 and shows good performance in terms of clinical application.

We next explored the clinical utility of the addition of the radiomics signature for each outcome to the models with only clinical data included. As shown in Table 3, the AUCs of the clinical models were 0.728, 0.952, 0.726, and 0.861 for the higher stage, death, complications, and ARDS prediction models, respectively. After combining the radiomics signatures and clinical parameters, the AUCs of the mixed models were 0.925, 0.990, 0.929, and 0.903 for the higher stage, death, complications, and ARDS prediction models, respectively. The AUCs of the mixed models were higher than the clinical models. In addition, a significantly increased NRI (stage: $P < 0.001$; death: $P = 0.013$; complications: $P < 0.001$; ARDS: $P < 0.001$) was found for the mixed models compared with the clinical models.

Discussion

In this study, we described a prediction model for COVID-19 based on radiomic signatures. Based on the first CT scan after hospitalization, we can predict the prognosis of these patients early with high accuracy and intervene where necessary.

COVID-19 can influence several tissues and lead to organ failure rapidly. It has a poor prognosis and a high mortality rate. A

chest CT combined with a positive molecular PCR test is the most important diagnostic method for COVID-19. Compared with tests conducted in standard laboratories, the CT scan procedure has a faster turnaround time and can provide more detailed information regarding lung damage severity and acute respiratory failure.[18,19] Features of CT images can present with ground-glass opacities, linear opacities, consolidation, bronchial wall thickening, lymph node enlargement, pericardial effusion, or pleural effusion. However, the CT characteristics in some stages are somewhat similar, such as in severe and critical cases. Therefore, a single qualitative radiological diagnosis cannot fully meet our needs to predict the prognosis of the disease. Radiomics features can quantitatively reflect the invisible details of the lesions. First-order features (e.g., entropy, skewness, and kurtosis) describe the distribution of the values of individual voxels without concern for spatial relationships. Second-order (texture) features describe the statistical interrelationships

Table 1. Clinical characteristics

Characteristics	Overall	Survival cases	Death cases
Sex, n (%)			
Female	86 (55.13)	81 (55.1)	5 (55.56)
Male	70 (44.87)	66 (44.9)	4 (44.44)
Age, mean (SD)	63.13 (14.14)	62.44 (14.14)	74.56 (8.35)
Smoking			
No	145 (94.16)	138 (93.88)	7 (100)
Yes	9 (5.84)	9 (6.12)	0 (0)
Clinical symptoms			
Fever, n (%)	96 (62.34)	92 (62.59)	4 (57.14)
Cough, n (%)	98 (63.64)	93 (63.27)	5 (71.43)
Chest pain, n (%)	40 (25.97)	37 (25.17)	3 (42.86)
Hypodynamia (%)	75 (48.7)	73 (49.66)	2 (28.57)
Diarrhea, n (%)	15 (9.74)	15 (10.2)	0 (0)
Comorbidities			
Diabetes, n (%)	35 (22.73)	34 (23.13)	1 (14.29)
HTN, n (%)	76 (49.35)	72 (48.98)	4 (57.14)
Respiratory diseases, n (%)	14 (9.09)	13 (8.84)	1 (14.29)
Heart diseases, n (%)	28 (18.3)	28 (19.18)	0 (0)
Tumors, n (%)	6 (3.9)	5 (3.4)	1 (14.29)
Stage, n (%)			
Mild	97 (62.18)	97 (65.99)	0 (0)
Severe	59 (37.82)	50 (34.01)	9 (100)
Complication, n (%)			
No	131 (83.97)	130 (88.44)	1 (11.11)
Yes	25 (16.03)	17 (11.56)	8 (88.89)
Respiratory failure, n (%)	19 (12.18)	13 (8.84)	6 (66.67)
ARDS, n (%)	11 (7.05)	5 (3.4)	6 (66.67)
Heart failure, n (%)	7 (4.49)	5 (3.4)	2 (22.22)
AKI, n (%)			
0	143 (91.67)	139 (94.56)	4 (44.44)
1	7 (4.49)	3 (2.04)	4 (44.44)
2	2 (1.28)	2 (1.36)	0 (0)
3	4 (2.56)	3 (2.04)	1 (11.11)
WBC, median (Q1, Q3)	5.92 (4.71, 7.29)	5.91 (4.7, 7.17)	6.48 (5.08, 10.36)
CRP, median (Q1, Q3)	2.91 (0.5, 19.66)	2.37 (0.5, 15.18)	40 (22.22, 108.8)
Lymphocyte, median (Q1, Q3)	1.33 (0.84, 1.75)	1.37 (0.88, 1.75)	0.54 (0.19, 0.72)
Time between onset of symptoms to admission, median (Q1, Q3)	22 (15, 30)	22 (15.5, 30.5)	20 (13, 23.75)

AKI, acute kidney injury; SD, standard deviation; WBC, white blood cells; CRP, C-reactive protein; ARDS, acute respiratory distress syndrome; HTN, hypertension.

between voxels with similar (or dissimilar) contrast values. Higher-order statistical methods impose filter grids on the image to extract repetitive or non-repetitive patterns. For instance, among the final selected features, firstorder_10Percentile indicated the 10th percentile of intensity in the ROI, which may reflect the relationship between the density of lesions and the disease grade.

Several studies on CT radiomics and the deep-learning technique have shown the efficiency of a rapid diagnosis of COVID-19. In a large cohort of 3,777 patients, the artificial intelligence diagnostic model can differentiate NCP from other common pneumonia with 92.49% accuracy, 94.93% sensitivity, 91.13% specificity, and an area under the ROC curve of 0.9797.[6] Another deep-learning artificial intelligence-enabled rapid diagnosis system also showed a clinical benefit. However, studies focusing on prognosis prediction using quantitative image features are rare. Our research was the first study to investigate the role of CT radiomics in predicting the prognosis of patients with COVID-19. The AUCs of each model demonstrated good predictive accuracy (0.85–0.92). The DCA also indicated

a good performance in terms of clinical application.

Several retrospective cohort studies have described the multi-organ damage caused by COVID-19, including respiratory, cardiovascular, digestive, urinary, endocrine, and nervous system damage.[20,21] Accurate predictive models are needed to identify the risk of patients experiencing a poor clinical outcome and plan early intervention to improve outcomes. Previous studies have found several variables that are risk factors for a severe prognosis related to COVID-19 and have built effective prediction models for patient management.[22,23] The following factors contain comprehensive clinical data: chest radiography abnormality, age, interleukin-6, dyspnea, number of comorbidities, cancer history, lower lymphocyte count, higher lactate dehydrogenase neutrophil-to-lymphocyte ratio, lactate dehydrogenase, creatinine, and direct bilirubin. However, these data rely on large data collection samples and patient follow ups for the entire study, which might lead to economic issues. In our preliminary study, the first CT image on arrival at the medical center could bring us more infor-

mation than chest lesions. An important advancement in the use of imaging is assisting clinical management in identifying high-risk groups and intervening early to reduce mortality. However, the lack of widely used CT scanning equipment and experienced radiologists might affect the clinical application of these prediction models. Similar to previous research, the data models used in the present research relied on accurate labeling by professional radiologists. Moreover, the clinical characteristics and outcomes were estimated by the expert radiologists for the description of the state of the patient but did not consider the real severity.[5] One limitation of this study is the small sample size for validation and the use of patients in the same country, which could cause bias. This retrospective study could also contain missing data. Additional prospective global multi-center validation studies of COVID-19 are recommended.

In conclusion, the radiomic signature provided vital information for predicting the prognosis of COVID-19. We built a model consisting of a radiomic signature that had maximum accuracy in the prediction of the
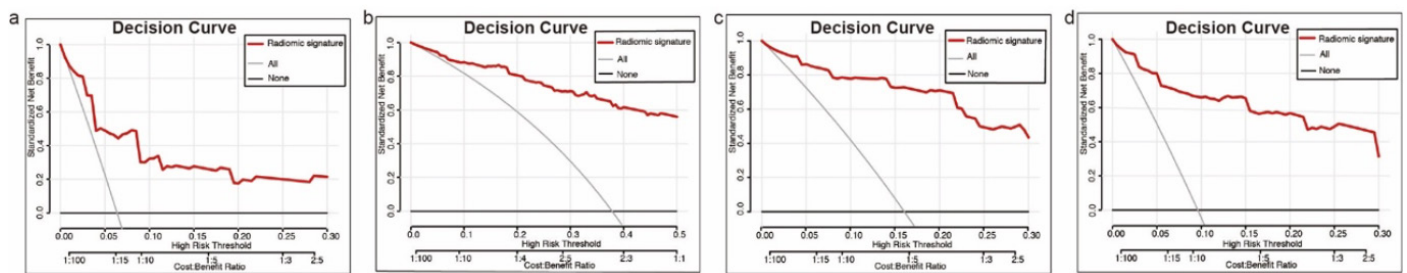
Figure 2. Predictive accuracy of the radiomic signature, as evaluated by the Harrell's C-index. **(a)** Predictive value for death; **(b)** predictive value for stage; **(c)** predictive value for complications; **(d)** predictive value for acute respiratory distress syndrome.

Table 2. AUC and NRI with the corresponding *P* value of the clinical models and mixed models for predicting the outcome and NRI value to compare COVID-19 patients

	AUC for the clinical model (SE, 95% CI)	AUC for the mixed models (SE, 95% CI)	NRI	*P* value[1]
Stage	0.728 (0.042, 0.646- 0.809)	0.925 (0.020, 0.885-0.966)	1.34	<0.001
Death	0.952 (0.018, 0.917-0.986)	0.990 (0.019, 0.953-1.000)	0.280	0.013
Complications	0.726 (0.056, 0.616-0.836)	0.929 (0.043, 0.844-0.969)	1.064	<0.001
ARDS	0.861 (0.058, 0.748-0.975)	0.903 (0.060, 0.786-1.000)	0.787	<0.001

[1]$P < 0.05$ indicated the calculated NRI was statistically significant. AUC, area under curve; SE, standard error; CI, confidence interval; NRI, net reclassification index; ARDS, acute respiratory distress syndrome; COVID-19, coronavirus disease-2019.

Table 3. Efficacy of the radiomic signature in the prediction of the outcome

Outcome	Harrell's C-index	C-index after bootstrap (95% CI)	Accuracy	Sensitivity	Specificity
Stage	0.918	0.919 (0.917–0.922)	0.814	0.949	0.732
Death	0.846	0.846 (0.844–0.848)	0.854	0.700	0.864
Complications	0.919	0.919 (0.916–0.921)	0.846	0.920	0.832
ARDS	0.852	0.853 (0.852–0.855)	0.814	0.818	0.814

CI, confidence interval; ARDS, acute respiratory distress syndrome.

prognosis. Our study provided vital insight into important preoperative clinical decisions and is expected to be applied in multiple medical centers to optimize future diagnoses and treatments.

Conflict of interest disclosure

The authors declared no conflicts of interest.

Funding

References

1. Guan WJ, Ni ZY, Hu Y, et al. Clinical characteristics of coronavirus disease 2019 in China. *N Engl J Med*. 2020;382(18):1708-1720. [CrossRef]

2. Majumder J, Minko T. Recent developments on therapeutic and diagnostic approaches for COVID-19. *AAPS J*. 2021;23(1):14. [CrossRef]

3. Wei W, Hu XW, Cheng Q, Zhao YM, Ge YQ. Identification of common and severe COVID-19: the value of CT texture analysis and correlation with clinical characteristics. *Eur Radiol*. 2020;30(12):6788-6796. [CrossRef]

4. Fang X, Kruger U, Homayounieh F, et al. Association of AI quantified COVID-19 chest CT and patient outcome. *Int J Comput Assist Radiol Surg*. 2021;16(3):435-445. [CrossRef]

5. Biondi R, Curti N, Coppola F, et al. Classification performance for COVID patient prognosis from automatic AI segmentation--a single-center study. *Appl Sci*. 2021; 11(12):5438. [CrossRef]

6. Zhang K, Liu X, Shen J, et al. Clinically applicable AI System for Accurate Diagnosis, Quantitative Measurements, and Prognosis of COVID-19 pneumonia using computed tomography. *Cell*. 2020;181(6):1423-1433. [CrossRef]

7. Huang P, Liu T, Huang L, et al. Use of chest CT in combination with negative RT-PCR assay for the 2019 novel coronavirus but high clinical suspicion. *Radiology*. 2020;295(1):22-23. [CrossRef]

8. Sun R, Limkin EJ, Vakalopoulou M, et al. A radiomics approach to assess tumour-infiltrating CD8 cells and response to anti-PD-1 or anti-PD-L1 immunotherapy: an imaging biomarker, retrospective multicohort study. *Lancet Oncol*. 2018;19(9):1180-1191. [CrossRef]

9. Lambin P, Leijenaar RTH, Deist TM, et al. Radiomics: the bridge between medical imaging and personalized medicine. *Nat Rev Clin Oncol*. 2017;14(12):749-762. [CrossRef]

10. van Griethuysen JJM, Fedorov A, Parmar C, et al. Computational radiomics system to decode the radiographic phenotype. *Cancer Res*. 2017;77(21):104-107. [CrossRef]

11. Zhang QW, Gao YJ, Zhang RY, et al. Personalized CT-based radiomics nomogram preoperative predicting Ki-67 expression in gastrointestinal stromal tumors: a multicenter development and validation cohort. *Clin Transl Med*. 2020;9(1):12. [CrossRef]

12. Zhang QW, Zhou XX, Zhang RY, et al. Comparison of malignancy-prediction efficiency between contrast and non-contract CT-based radiomics features in gastrointestinal stromal tumors: a multicenter study. *Clin Transl Med*. 2020;10(3):e291. [CrossRef]

13. Fluss R, Faraggi D, Reiser B. Estimation of the Youden index and its associated cutoff point. *Biom J*. 2005;47(4):458-472. [CrossRef]

14. Smith PJ, Hoaglin DC, Battaglia MP, Barker L, et al. Implementation and applications of bootstrap methods for the National Immunization Survey. *Stat Med*. 2003;22(15): 2487-2502. [CrossRef]

15. Vickers AJ, Van Calster B, Steyerberg EW. Net benefit approaches to the evaluation of prediction models, molecular markers, and diagnostic tests. *BMJ*. 2016;352:i6. [CrossRef]

16. Uno H, Tian L, Cai T, Kohane IS, Wei LJ. A unified inference procedure for a class of measures to assess improvement in risk prediction systems with survival data. *Stat Med*. 2013;32(14):2430-2442. [CrossRef]

17. De Jay N, Papillon-Cavanagh S, Olsen C, El-Hachem N, Bontempi G, Haibe-Kains B. mRMRe: an R package for parallelized mRMR ensemble feature selection. *Bioinformatics*. 2013;29(18):2365-2368. [CrossRef]

18. Shi H, Han X, Jiang N, et al. Radiological findings from 81 patients with COVID-19 pneumonia in Wuhan, China: a descriptive study. *Lancet Infect Dis*. 2020;20(4):425-434. [CrossRef]

19. Yang X, Yu Y, Xu J, et al. Clinical course and outcomes of critically ill patients with SARS-CoV-2 pneumonia in Wuhan, China: a single-centered, retrospective, observational study. *Lancet Respir Med*. 2020;8(5):475-481. [CrossRef]

20. Wu C, Chen X, Cai Y et al. Risk factors associated with acute respiratory distress syndrome and death in patients with coronavirus disease 2019 pneumonia in Wuhan, China. *JAMA Intern Med*. 2020;180(7):934-943. [CrossRef]

21. Wu Z, McGoogan JM. Characteristics of and important lessons from the coronavirus disease 2019 (COVID-19) outbreak in China: summary of a report of 72 314 cases from the Chinese Center for Disease Control and Prevention. *JAMA*. 2020;323(13):1239-1242. [CrossRef]

22. Liang W, Liang H, Ou L, et al. Development and validation of a clinical risk score to predict the occurrence of critical illness in hospitalized patients with COVID-19. *JAMA Intern Med*. 2020;180(8):1081-1089. [CrossRef]

23. Zhou F, Yu T, Du R, et al. Clinical course and risk factors for mortality of adult inpatients with COVID-19 in Wuhan, China: a retrospective cohort study. *Lancet*. 2020;395(10229):1054-1062. [CrossRef]

Supplementary Table 1. Results of paired samples t-test and interclass or intraclass correlation coefficient calculations for radiomics paramaters

Paramater	Inter-class correlation coefficients		Paired samples t-test	
	Same researcher at different time	Different researcher at same time	Same researcher at different time	Different researcher at same time
original_firstorder_10Percentile	0.999997	0.998569	0.340784	0.89771
original_firstorder_90Percentile	0.931262	0.912729	0.077749	0.29402
original_firstorder_Energy	0.981199	0.951514	0.104202	0.77724
original_firstorder_Entropy	0.976015	0.86105	0.081715	0.773565
original_firstorder_InterquartileRange	0.970405	0.894157	0.211248	0.899302
original_firstorder_Kurtosis	0.804423	0.816997	0.027186	0.150026
original_firstorder_Mean	0.998257	0.996387	0.09966	0.616588
original_firstorder_MeanAbsoluteDeviation	0.956756	0.854623	0.071953	0.490757
original_firstorder_Median	0.999905	0.998343	0.33764	0.579896
original_firstorder_Minimum	0.999795	0.970584	0.305204	0.994862
original_firstorder_Range	0.985947	0.881659	0.259128	0.710139
original_firstorder_RobustMeanAbsoluteDeviation	0.947647	0.876259	0.126852	0.726577
original_firstorder_RootMeanSquared	0.997488	0.993777	0.091024	0.565349
original_firstorder_Skewness	0.902097	0.93577	0.040829	0.369576
original_firstorder_TotalEnergy	0.981199	0.951514	0.104202	0.77724
original_firstorder_Uniformity	0.989356	0.818425	0.067482	0.994303
original_firstorder_Variance	0.981203	0.847101	0.09128	0.458786
original_glcm_Autocorrelation	0.986151	0.892283	0.2128	0.902616
original_glcm_ClusterProminence	0.989671	0.893246	0.29526	0.433852
original_glcm_ClusterShade	0.988522	0.890284	0.208842	0.379651
original_glcm_ClusterTendency	0.981285	0.869552	0.094478	0.477418
original_glcm_Contrast	0.99549	0.803835	0.10815	0.531676
original_glcm_DifferenceVariance	0.994748	0.807939	0.09233	0.53265
original_glcm_JointAverage	0.993272	0.825104	0.121628	0.937817
original_glcm_SumEntropy	0.978179	0.89127	0.077978	0.793367
original_glcm_SumSquares	0.983116	0.864382	0.094545	0.479741
original_gldm_DependenceEntropy	0.976726	0.853071	0.073941	0.817061
original_gldm_GrayLevelNonUniformity	0.998773	0.872752	0.049065	0.957319
original_gldm_GrayLevelVariance	0.981222	0.847155	0.091383	0.458466
original_gldm_HighGrayLevelEmphasis	0.985763	0.887965	0.200588	0.850271
original_gldm_SmallDependenceHighGrayLevelEmphasis	0.990101	0.899873	0.247325	0.48425
original_glrlm_GrayLevelNonUniformityNormalized	0.919503	0.939251	0.064681	0.603984
original_glrlm_GrayLevelVariance	0.980288	0.868816	0.071361	0.478433
original_glrlm_HighGrayLevelRunEmphasis	0.983907	0.90651	0.149272	0.851096
original_glrlm_LongRunHighGrayLevelEmphasis	0.973192	0.899739	0.316009	0.928954
original_glrlm_ShortRunHighGrayLevelEmphasis	0.983982	0.905354	0.144339	0.790248
original_glszm_GrayLevelNonUniformity	0.997252	0.828012	0.138214	0.565119
original_glszm_GrayLevelVariance	0.993678	0.816953	0.076984	0.464003
original_glszm_HighGrayLevelZoneEmphasis	0.987263	0.926078	0.107404	0.683375
original_glszm_SizeZoneNonUniformity	0.997713	0.887896	0.052518	0.378143
original_glszm_SizeZoneNonUniformityNormalized	0.995576	0.968844	0.954024	0.794447
original_glszm_SmallAreaEmphasis	0.994757	0.960487	0.825246	0.867285
original_glszm_SmallAreaHighGrayLevelEmphasis	0.990794	0.93481	0.132973	0.643441
original_glszm_ZonePercentage	0.996098	0.822963	0.090173	0.608169
original_ngtdm_Complexity	0.996361	0.872722	0.377178	0.592898

Paramater	Inter-class correlation coefficients		Paired samples t-test	
	Same researcher at different time	Different researcher at same time	Same researcher at different time	Different researcher at same time
original_shape_Flatness	0.990597	0.82496	0.250526	0.609563
original_shape_LeastAxisLength	0.99722	0.943945	0.314855	0.662473
original_shape_MajorAxisLength	0.999914	0.995239	0.04126	0.453035
original_shape_Maximum2DDiameterColumn	0.997574	0.979956	0.121475	0.595147
original_shape_Maximum2DDiameterSlice	0.999441	0.997251	0.221079	0.093845
original_shape_Maximum3DDiameter	0.990835	0.933314	0.523592	0.572199
original_shape_MeshVolume	0.992537	0.979207	0.094729	0.745679
original_shape_MinorAxisLength	0.993714	0.987656	0.183195	0.787999
original_shape_Sphericity	0.993593	0.963324	0.863871	0.437983
original_shape_SurfaceArea	0.991339	0.967048	0.102698	0.902472
original_shape_SurfaceVolumeRatio	0.99673	0.97189	0.207659	0.89069
original_shape_VoxelVolume	0.992549	0.97913	0.095193	0.747323
wavelet.HHH_firstorder_Energy	0.992533	0.978802	0.091866	0.74983
wavelet.HHH_firstorder_Entropy	0.9976	0.853074	0.339822	0.570975
wavelet.HHH_firstorder_Kurtosis	0.987216	0.943184	0.108393	0.801723
wavelet.HHH_firstorder_Mean	0.956551	0.870222	0.07011	0.988223
wavelet.HHH_firstorder_RootMeanSquared	0.983791	0.881095	0.070903	0.634193
wavelet.HHH_firstorder_TotalEnergy	0.992533	0.978802	0.091866	0.74983
wavelet.HHH_firstorder_Uniformity	0.996915	0.867726	0.340438	0.575115
wavelet.HHH_glcm_SumSquares	0.996365	0.873037	0.333482	0.578942
wavelet.HHH_gldm_DependenceNonUniformity	0.993546	0.903916	0.093858	0.592758
wavelet.HHH_gldm_GrayLevelNonUniformity	0.992541	0.979206	0.095415	0.750379
wavelet.HHH_gldm_GrayLevelVariance	0.997083	0.872956	0.340921	0.589302
wavelet.HHH_glrlm_GrayLevelNonUniformity	0.992771	0.952948	0.09509	0.663165
wavelet.HHH_glrlm_GrayLevelNonUniformityNormalized	0.997063	0.868934	0.28946	0.565452
wavelet.HHH_glrlm_GrayLevelVariance	0.997263	0.875035	0.327481	0.584239
wavelet.HHH_glrlm_RunLengthNonUniformity	0.993162	0.909943	0.09408	0.606215
wavelet.HHH_glszm_GrayLevelNonUniformity	0.997211	0.924464	0.1783	0.501813
wavelet.HHH_glszm_SizeZoneNonUniformity	0.994287	0.898315	0.614822	0.517346
wavelet.HHH_glszm_ZonePercentage	0.994332	0.890479	0.582649	0.498157
wavelet.HHH_ngtdm_Coarseness	0.995103	0.922732	0.295053	0.577228
wavelet.HHL_firstorder_Energy	0.992573	0.97842	0.095536	0.752877
wavelet.HHL_firstorder_Kurtosis	0.995111	0.934285	0.128894	0.58736
wavelet.HHL_firstorder_Mean	0.958346	0.983521	0.061073	0.284902
wavelet.HHL_firstorder_TotalEnergy	0.992573	0.97842	0.095536	0.752877
wavelet.HHL_glcm_ClusterProminence	0.995852	0.826601	0.386051	0.81669
wavelet.HHL_gldm_SmallDependenceHighGrayLevelEmphasis	0.999973	0.869799	0.37208	0.478685
wavelet.HHL_ngtdm_Coarseness	0.997978	0.818081	0.373987	0.668612
wavelet.HHL_ngtdm_Complexity	0.999973	0.836216	0.90023	0.613464
wavelet.HLH_firstorder_Energy	0.992497	0.978972	0.09724	0.760804
wavelet.HLH_firstorder_Mean	0.812382	0.841375	0.254883	0.913161
wavelet.HLH_firstorder_TotalEnergy	0.992497	0.978972	0.09724	0.760804
wavelet.HLH_firstorder_Variance	0.999676	0.800837	0.309301	0.523766
wavelet.HLH_glcm_ClusterProminence	0.997213	0.964836	0.25719	0.19153
wavelet.HLH_glcm_DifferenceVariance	0.998513	0.808758	0.731429	0.454816

Supplementary Table 1. Continues

Paramater	Inter-class correlation coefficients		Paired samples t-test	
	Same researcher at different time	Different researcher at same time	Same researcher at different time	Different researcher at same time
wavelet.HLH_gldm_GrayLevelNonUniformity	0.992458	0.980414	0.096699	0.831004
wavelet.HLH_gldm_GrayLevelVariance	0.998752	0.851739	0.347758	0.344964
wavelet.HLH_gldm_LargeDependenceHighGrayLevelEmphasis	0.999988	0.809386	0.543159	0.65892
wavelet.HLH_gldm_SmallDependenceHighGrayLevelEmphasis	0.999972	0.825346	0.581967	0.565302
wavelet.HLH_glrlm_GrayLevelNonUniformity	0.994352	0.85521	0.095236	0.699494
wavelet.HLH_glrlm_GrayLevelVariance	0.998828	0.860282	0.385184	0.343714
wavelet.HLH_glszm_SizeZoneNonUniformity	0.998773	0.827246	0.048067	0.326173
wavelet.HLH_glszm_SmallAreaHighGrayLevelEmphasis	0.984661	0.803754	0.267622	0.857598
wavelet.HLH_glszm_ZonePercentage	0.996543	0.810394	0.135219	0.334475
wavelet.HLH_ngtdm_Coarseness	0.995668	0.836895	0.215283	0.564965
wavelet.HLH_ngtdm_Complexity	0.999999	0.815922	0.710351	0.649103
wavelet.HLH_ngtdm_Strength	0.999796	0.918313	0.395136	0.77281
wavelet.HLL_firstorder_Energy	0.992859	0.978	0.091609	0.727026
wavelet.HLL_firstorder_Mean	0.970284	0.962328	0.091242	0.299141
wavelet.HLL_firstorder_Median	0.988699	0.949159	0.294879	0.531518
wavelet.HLL_firstorder_RootMeanSquared	0.997913	0.896491	0.076846	0.689229
wavelet.HLL_firstorder_TotalEnergy	0.992859	0.978	0.091609	0.727026
wavelet.HLL_glcm_Idn	0.999305	0.895923	0.41531	0.670298
wavelet.HLL_glrlm_GrayLevelNonUniformity	0.997355	0.830152	0.114151	0.692293
wavelet.HLL_glszm_LargeAreaHighGrayLevelEmphasis	0.959884	0.801546	0.146286	0.490789
wavelet.HLL_ngtdm_Coarseness	0.998071	0.920443	0.450353	0.670578
wavelet.LHH_firstorder_Energy	0.992543	0.978972	0.10106	0.760804
wavelet.LHH_firstorder_Entropy	0.999483	0.858038	0.397848	0.461672
wavelet.LHH_firstorder_Kurtosis	0.986817	0.936929	0.068087	0.951105
wavelet.LHH_firstorder_Mean	0.983004	0.963404	0.965327	0.384285
wavelet.LHH_firstorder_Median	0.837757	0.883881	0.883249	0.7669
wavelet.LHH_firstorder_RootMeanSquared	0.969978	0.840774	0.990503	0.404368
wavelet.LHH_firstorder_TotalEnergy	0.992543	0.978972	0.10106	0.760804
wavelet.LHH_firstorder_Uniformity	0.99912	0.871824	0.258251	0.448879
wavelet.LHH_firstorder_Variance	0.999802	0.816434	0.245848	0.586159
wavelet.LHH_glcm_ClusterProminence	0.998194	0.848527	0.221417	0.523894
wavelet.LHH_glcm_DifferenceEntropy	0.99955	0.838622	0.935167	0.642927
wavelet.LHH_glcm_DifferenceVariance	0.999334	0.879789	0.960564	0.655147
wavelet.LHH_glcm_JointEntropy	0.999484	0.854578	0.663912	0.515146
wavelet.LHH_glcm_SumSquares	0.999241	0.889891	0.399138	0.42814
wavelet.LHH_gldm_DependenceNonUniformity	0.993966	0.900768	0.102525	0.710826
wavelet.LHH_gldm_GrayLevelNonUniformity	0.992463	0.979784	0.09628	0.788401
wavelet.LHH_gldm_GrayLevelVariance	0.999191	0.884752	0.349828	0.435273
wavelet.LHH_gldm_LargeDependenceHighGrayLevelEmphasis	0.98298	0.83397	0.338624	0.63401
wavelet.LHH_glrlm_GrayLevelNonUniformity	0.994184	0.840796	0.099308	0.662251
wavelet.LHH_glrlm_GrayLevelNonUniformityNormalized	0.999397	0.878896	0.371097	0.426207
wavelet.LHH_glrlm_GrayLevelVariance	0.999255	0.887979	0.392979	0.429678
wavelet.LHH_glrlm_LongRunHighGrayLevelEmphasis	0.980785	0.813507	0.338373	0.630056

Supplementary Table 1. Continues				
	Inter-class correlation coefficients		Paired samples t-test	
Paramater	Same researcher at different time	Different researcher at same time	Same researcher at different time	Different researcher at same time
wavelet.LHH_glszm_ZonePercentage	0.999538	0.88587	0.805809	0.328586
wavelet.LHH_ngtdm_Coarseness	0.994722	0.827216	0.254063	0.579548
wavelet.LHH_ngtdm_Complexity	0.998412	0.862594	0.344281	0.54478
wavelet.LHH_ngtdm_Strength	0.999182	0.950617	0.518519	0.698336
wavelet.LHL_firstorder_Energy	0.992982	0.977993	0.09054	0.737466
wavelet.LHL_firstorder_Kurtosis	0.985251	0.960151	0.21718	0.576139
wavelet.LHL_firstorder_Mean	0.989189	0.975507	0.206571	0.432871
wavelet.LHL_firstorder_Median	0.993039	0.960395	0.381912	0.757776
wavelet.LHL_firstorder_RootMeanSquared	0.998785	0.900936	0.269623	0.919027
wavelet.LHL_firstorder_TotalEnergy	0.992982	0.977993	0.09054	0.737466
wavelet.LHL_glcm_ClusterProminence	0.999094	0.821714	0.481395	0.962621
wavelet.LHL_glcm_Idn	0.988052	0.829679	0.243423	0.301559
wavelet.LHL_glcm_Imc2	0.921777	0.884274	0.075303	0.464799
wavelet.LHL_gldm_SmallDependenceHighGrayLevelEmphasis	0.999981	0.922039	0.10615	0.917856
wavelet.LHL_glrlm_LongRunHighGrayLevelEmphasis	0.994766	0.829221	0.123789	0.630026
wavelet.LHL_glrlm_RunEntropy	0.992932	0.814147	0.077034	0.935768
wavelet.LHL_glszm_SmallAreaHighGrayLevelEmphasis	0.99991	0.819829	0.10075	0.814189
wavelet.LHL_ngtdm_Coarseness	0.997763	0.907867	0.34602	0.687538
wavelet.LHL_ngtdm_Complexity	0.999964	0.847661	0.353431	0.842677
wavelet.LLH_firstorder_10Percentile	0.978338	0.861756	0.2552	0.586535
wavelet.LLH_firstorder_90Percentile	0.999921	0.972858	0.911368	0.826339
wavelet.LLH_firstorder_Energy	0.992656	0.979233	0.092076	0.736285
wavelet.LLH_firstorder_Entropy	0.999675	0.971114	0.1583	0.572401
wavelet.LLH_firstorder_InterquartileRange	0.998833	0.951668	0.278588	0.684967
wavelet.LLH_firstorder_Kurtosis	0.955345	0.956023	0.115104	0.195984
wavelet.LLH_firstorder_Maximum	0.999904	0.952952	0.167866	0.55534
wavelet.LLH_firstorder_Mean	0.957527	0.906466	0.352751	0.642735
wavelet.LLH_firstorder_MeanAbsoluteDeviation	0.999102	0.954881	0.228338	0.698042
wavelet.LLH_firstorder_Median	0.965658	0.885736	0.730984	0.925662
wavelet.LLH_firstorder_Minimum	0.999988	0.806223	0.343436	0.397651
wavelet.LLH_firstorder_Range	0.999979	0.912403	0.085281	0.639698
wavelet.LLH_firstorder_RobustMeanAbsoluteDeviation	0.99889	0.95315	0.286438	0.677357
wavelet.LLH_firstorder_RootMeanSquared	0.964063	0.922758	0.354273	0.655446
wavelet.LLH_firstorder_TotalEnergy	0.992656	0.979233	0.092076	0.736285
wavelet.LLH_firstorder_Uniformity	0.998027	0.963139	0.227154	0.554834
wavelet.LLH_firstorder_Variance	0.999634	0.96951	0.221421	0.474875
wavelet.LLH_glcm_ClusterProminence	0.999958	0.979225	0.339388	0.321153
wavelet.LLH_glcm_ClusterShade	0.992615	0.979219	0.901948	0.909563
wavelet.LLH_glcm_ClusterTendency	0.999786	0.986402	0.282204	0.274228
wavelet.LLH_glcm_DifferenceVariance	0.999782	0.803254	0.249572	0.697979
wavelet.LLH_glcm_Idmn	0.999972	0.800171	0.330608	0.226989
wavelet.LLH_glcm_Idn	0.999875	0.949396	0.299252	0.042735
wavelet.LLH_glcm_JointEnergy	0.999321	0.803753	0.252054	0.908083
wavelet.LLH_glcm_JointEntropy	0.999815	0.929506	0.172814	0.723083
wavelet.LLH_glcm_SumEntropy	0.999791	0.95771	0.186376	0.744586

Supplementary Table 1. Continues

Paramater	Inter-class correlation coefficients		Paired samples t-test	
	Same researcher at different time	Different researcher at same time	Same researcher at different time	Different researcher at same time
wavelet.LLH_gldm_DependenceNonUniformity	0.989604	0.823667	0.121778	0.686674
wavelet.LLH_gldm_DependenceVariance	0.990269	0.963407	0.354859	0.165496
wavelet.LLH_gldm_GrayLevelNonUniformity	0.992945	0.984785	0.103752	0.779552
wavelet.LLH_gldm_GrayLevelVariance	0.999734	0.973184	0.199483	0.380729
wavelet.LLH_gldm_SmallDependenceEmphasis	0.995889	0.835482	0.263067	0.779956
wavelet.LLH_glrlm_GrayLevelNonUniformityNormalized	0.999866	0.978885	0.213947	0.60723
wavelet.LLH_glrlm_GrayLevelVariance	0.999868	0.979676	0.302364	0.418486
wavelet.LLH_glszm_GrayLevelNonUniformity	0.945718	0.850553	0.034748	0.978811
wavelet.LLH_glszm_GrayLevelVariance	0.970813	0.839983	0.113992	0.664453
wavelet.LLH_glszm_SizeZoneNonUniformity	0.984696	0.855923	0.091929	0.844812
wavelet.LLH_glszm_ZonePercentage	0.992001	0.912203	0.202902	0.849231
wavelet.LLH_ngtdm_Complexity	1	0.833586	0.359565	0.608493
wavelet.LLH_ngtdm_Strength	0.999846	0.810294	0.347613	0.332152
wavelet.LLL_firstorder_10Percentile	0.999997	0.999439	0.301835	0.710013
wavelet.LLL_firstorder_90Percentile	0.934659	0.923225	0.078896	0.281365
wavelet.LLL_firstorder_Energy	0.972452	0.950174	0.106066	0.819672
wavelet.LLL_firstorder_Entropy	0.974177	0.918957	0.083673	0.798059
wavelet.LLL_firstorder_InterquartileRange	0.968017	0.912124	0.202452	0.847176
wavelet.LLL_firstorder_Maximum	0.956997	0.815744	0.160508	0.566333
wavelet.LLL_firstorder_Mean	0.998299	0.996389	0.099534	0.618757
wavelet.LLL_firstorder_MeanAbsoluteDeviation	0.954272	0.872252	0.072324	0.453276
wavelet.LLL_firstorder_Median	0.999906	0.998387	0.332724	0.550646
wavelet.LLL_firstorder_Minimum	1	0.987012	1	0.879349
wavelet.LLL_firstorder_Range	0.984956	0.927874	0.160508	0.659921
wavelet.LLL_firstorder_RobustMeanAbsoluteDeviation	0.943418	0.896723	0.123869	0.697487
wavelet.LLL_firstorder_RootMeanSquared	0.994469	0.985452	0.084579	0.524268
wavelet.LLL_firstorder_Skewness	0.89596	0.952381	0.042098	0.292629
wavelet.LLL_firstorder_TotalEnergy	0.972452	0.950174	0.106066	0.819672
wavelet.LLL_firstorder_Uniformity	0.989123	0.896448	0.066958	0.736956
wavelet.LLL_firstorder_Variance	0.979827	0.857975	0.091453	0.448699
wavelet.LLL_glcm_Autocorrelation	0.99588	0.901572	0.113141	0.914279
wavelet.LLL_glcm_ClusterProminence	0.988996	0.897991	0.295485	0.442857
wavelet.LLL_glcm_ClusterShade	0.988002	0.892853	0.209302	0.383499
wavelet.LLL_glcm_ClusterTendency	0.980493	0.875003	0.093982	0.470409
wavelet.LLL_glcm_Contrast	0.993183	0.863679	0.100833	0.49317
wavelet.LLL_glcm_DifferenceAverage	0.987753	0.818154	0.101494	0.668156
wavelet.LLL_glcm_DifferenceVariance	0.993249	0.861779	0.087696	0.483506
wavelet.LLL_glcm_InverseVariance	0.97276	0.811101	0.132027	0.502651
wavelet.LLL_glcm_JointAverage	0.996637	0.88368	0.096733	0.894735
wavelet.LLL_glcm_JointEntropy	0.983888	0.829103	0.090435	0.860867
wavelet.LLL_glcm_SumEntropy	0.975198	0.941017	0.08001	0.772539
wavelet.LLL_glcm_SumSquares	0.981578	0.874546	0.093701	0.470034
wavelet.LLL_gldm_DependenceEntropy	0.95646	0.973771	0.072763	0.671473
wavelet.LLL_gldm_DependenceNonUniformity	0.991417	0.837811	0.120744	0.520914
wavelet.LLL_gldm_DependenceNonUniformityNormalized	0.996895	0.807106	0.240026	0.695228

Paramater	Inter-class correlation coefficients		Paired samples t-test	
	Same researcher at different time	Different researcher at same time	Same researcher at different time	Different researcher at same time
wavelet.LLL_gldm_HighGrayLevelEmphasis	0.994784	0.896677	0.115249	0.853046
wavelet.LLL_gldm_LargeDependenceHighGrayLevelEmphasis	0.993485	0.807918	0.61861	0.180537
wavelet.LLL_gldm_SmallDependenceEmphasis	0.97975	0.816085	0.122701	0.700424
wavelet.LLL_gldm_SmallDependenceHighGrayLevelEmphasis	0.99369	0.903136	0.14232	0.508733
wavelet.LLL_gldm_SmallDependenceLowGrayLevelEmphasis	0.999841	0.847811	0.492586	0.315844
wavelet.LLL_glrlm_GrayLevelNonUniformity	0.996362	0.998659	0.047327	0.478971
wavelet.LLL_glrlm_GrayLevelNonUniformityNormalized	0.972085	0.945134	0.063713	0.951928
wavelet.LLL_glrlm_GrayLevelVariance	0.979409	0.864066	0.081358	0.442235
wavelet.LLL_glrlm_HighGrayLevelRunEmphasis	0.993533	0.905425	0.100201	0.810979
wavelet.LLL_glrlm_LongRunHighGrayLevelEmphasis	0.994926	0.885049	0.11525	0.760629
wavelet.LLL_glrlm_RunEntropy	0.910947	0.982523	0.076571	0.296386
wavelet.LLL_glrlm_ShortRunHighGrayLevelEmphasis	0.993121	0.906709	0.101465	0.756248
wavelet.LLL_glszm_GrayLevelNonUniformity	0.994386	0.859811	0.384187	0.822736
wavelet.LLL_glszm_GrayLevelVariance	0.99037	0.868936	0.094182	0.45735
wavelet.LLL_glszm_HighGrayLevelZoneEmphasis	0.991484	0.921692	0.082135	0.635025
wavelet.LLL_glszm_LargeAreaHighGrayLevelEmphasis	0.968182	0.89771	0.043252	0.058174
wavelet.LLL_glszm_SizeZoneNonUniformity	0.985194	0.91284	0.066956	0.382645
wavelet.LLL_glszm_SizeZoneNonUniformityNormalized	0.981661	0.964778	0.077366	0.291391
wavelet.LLL_glszm_SmallAreaEmphasis	0.979067	0.96374	0.086227	0.322612
wavelet.LLL_glszm_SmallAreaHighGrayLevelEmphasis	0.99303	0.926193	0.080552	0.571575
wavelet.LLL_glszm_ZonePercentage	0.975948	0.805756	0.132691	0.739583
wavelet.LLL_ngtdm_Coarseness	0.999928	0.810494	0.318255	0.507877
wavelet.LLL_ngtdm_Complexity	0.997228	0.910728	0.414899	0.626529
wavelet.LLL_ngtdm_Strength	0.979982	0.94111	0.509235	0.962508